HEAVY ION ORBITING AND REGGE POLES (III)

F. CARSTOIU[1], M. LASSAUT[2], L. TRACHE[1], V. BALANICA[1]

[1]Horia Hulubei National Institute for Nuclear Physics and Engineering,
P.O.B. MG-6, RO-077125, Bucharest-Magurele, Romania
[2]Institut de Physique Nucléaire, CNRS-IN2P3, Univ. Paris-Sud,
Université Paris-Saclay, 91406 Orsay Cedex, France

Received March 8, 2016

We discuss two reactions initiated by the loosely bounded ^{6}Li in an energy window where the interaction with light targets is strongly refractive and moderately absorbing. The surface transparency of the optical potential allows a considerable internal barrier component of the scattering amplitude which leads to significant refractive effects and diffractive scattering at large angles due to Regge poles located near the real axis, close to the orbiting momentum. The folding potentials based on realistic effective NN interactions revealed a number of phase equivalent discrete solutions with real volume integrals close to the bare potential values ($N_v \approx 1$). This suggests that the real part of the dynamic polarization potential arising from the coupling to the breakup channel is small.

Key words: G-matrix effective interactions, folding potentials, WKB, Regge poles, orbiting.

PACS: 24.10.Ht, 25.55.Ci, 25.70.Ef.

1. INTRODUCTION

We discuss here two reactions initiated by ^{6}Li in an energy window where the interaction with light targets is strong and moderately absorptive. The interaction shows sufficient surface transparency to allow strong refractive effects superimposed on diffractive effects due to strong absorption at forward angles and Regge poles at large angles. Our basic approach for analysis is the folding potential as a first order approximation of the mean field in the sense of the reaction theory of Feshbach [1]. We adhere to the empirical finding that the complex second order potential, the so called Dynamic Polarization Potential (DPP), which arise from the coupling to inelastic channels is dominantly imaginary and has a large effect mostly on the range of total potential. Indeed, all phenomenological analyzes of the heavy ion elastic scattering found that $R_v < R_w$, where $R_{v,w}$ are the radii of the real and imaginary component of the optical potential. We use folding form factors for both real and imaginary components of the optical potential,

$$U(R) = N_v V(R, t_v) + iN_w V(R, t_w) \tag{1}$$

where $N_{v,w}$ are normalization constants and $t_{v,w}$ are range parameters defined by the scaling transformation,

$$V(R,t) \rightarrow t^3 V_{fold}(tR) \tag{2}$$

This transformation conserves the volume integral of the folding potential and modifies the radius as,

$$< R^2 >_V = \frac{1}{t^2} < R^2 >_{fold} \tag{3}$$

If our approximation has a physical meaning then we should find $t_v \approx 1$ and large corrections for t_w. Besides a huge computing time saving, the scaling transformation defined above allowed a full exploration of the parameter space N_v, N_w, t_v, t_w. In this way we found for each reaction a sequence of phase equivalent solutions, common to all effective interaction used, and with real normalization $N_v \rightarrow 1$. In the particular case of the loosely bound ^{6}Li, for which the coupling to the breakup channel could be important, the existence of solutions with volume integrals close to the bare potential values ($N_v \approx 1$), some care should be taken in obtaining the DPP from a CCDC calculation [2].

On a theoretical point of view, the discrete ambiguities have been investigated for complex potentials by Sabatier [3] and Cuer [4] in the framework of the WKB method. A physical interpretation has been given by Leeb and Schmid [5], in which the occurrence of discrete ambiguities is linked to the existence of partly Pauli forbidden states. For real potentials, Loeffel [6] has obtained theorems ensuring a unique potential from the knowledge of the phase-shifts δ_ℓ for all (non-discrete) non negative values of $\lambda = \ell + 1/2$. If the data set reduces to discrete values of $\lambda = \ell + 1/2$ for non-negative integer ℓ, the Carlson's theorem [7] predicts a unique potential $V(r)$, provided it belongs to a suitable class [6, 8]. In this case the ambiguities are due to the fact that we have at our disposition only a finite number of phase-shifts $\delta_\ell, \ell = 0, 1, .., N$. A class of real phase-equivalent potentials reproducing the phase-shifts $\delta_\ell, \ell = 0, 1, .., N$ has been constructed in [9].

As remarked by Brandan and Satchler [10] the knock-on exchange contribution to the folding potential is far from negligible when realistic nucleon-nucleon interactions are used. The relative sizes of the direct and exchange terms are sensitive to the effective interaction chosen between two nucleons in odd states of relative motion. This occurs because the odd-state components yield direct and exchange terms of opposite sign. A typical example is the well known G-matrix effective interaction in his Reid or Paris variants. The older Reid-based interaction results in an attractive direct component, and an attractive exchange component of similar magnitude. On the other hand, the more realistic Paris-based interaction results in a repulsive direct potential. This is compensated for by a much more attractive exchange term, such that the summed direct plus exchange potentials from the two interactions are almost identical. This points to a proper manipulation of the exchange kernels.

Finally, we show that the high surface transparency of the potential allows a strong internal barrier component of the scattering amplitude with repeated reflections between the most internal (centrifugal) turning point and the barrier turning point, and thus important refractive/resonant effects such as orbiting to be identified.

2. ^{6}LI+^{12}C AT 30.6 MeV

Table 1
A standard WS[1] solution for the reaction ^{6}Li+^{12}C at 30.6 MeV. The reduced radii are defined in the heavy ion convention. $J_{v,w}$ are volume integrals per interacting nucleon pair and $R_{v,w}$ are the rms radii of the potential.

V	W	r_v	r_w	r_c	a_v	a_w	χ^2	σ_R	J_v	R_v	J_w	R_w
204.	7.53	0.5842	1.2594	1.0	0.8844	0.5851	5.06	1189.	387.	3.7710	68.	4.5583

Table 2
Discrete folding solutions for the reaction ^{6}Li+^{12}C at 30.6 MeV. $N_{v,w}$ are normalization parameters, $t_{v,w}$ are scaling range parameters [16], $J_{v,w}$ are normalized volume integrals and $R_{v,w}$ are rms radii.

pot	N_v	N_w	t_v	t_w	χ^2	σ_R	J_v	R_v	J_w	R_w
	0.5700	0.1305	1.0075	0.7328	6.03	1340.	260.53	3.741	58.48	5.125
M3YZR	0.8100	0.1332	1.0460	0.8126	3.30	1246.	371.27	3.605	60.04	4.627
	1.0550	0.1432	1.0806	0.8547	3.48	1223.	484.78	3.491	64.74	4.401
	0.5000	0.1094	1.0077	0.7759	8.77	1285.	275.03	3.791	59.21	4.908
M3YFR	0.7000	0.1131	1.0512	0.8456	5.18	1213.	386.23	3.636	61.49	4.508
	0.9100	0.1227	1.0876	0.8801	5.89	1197.	503.39	3.516	66.88	4.333
	0.4300	0.0925	1.0092	0.7915	10.24	1265.	280.70	3.808	59.47	4.840
GOGNY1	0.6050	0.0970	1.0503	0.8568	7.70	1204.	396.07	3.661	62.62	4.476
	0.7900	0.1071	1.0871	0.8831	8.64	1198.	518.51	3.539	69.33	4.344
	0.4150	0.3745	0.9644	0.8066	6.99	1237.	271.45	3.775	58.18	4.826
JLM1	0.5900	0.4002	1.0000	0.8695	5.22	1191.	386.94	3.643	62.44	4.481
	0.7750	0.4385	1.0272	0.9062	6.58	1181.	509.30	3.547	68.59	4.303
	0.4500	0.4597	0.9571	0.7990	5.18	1249.	269.30	3.769	57.27	4.853
JLM3	0.6350	0.4860	0.9942	0.8620	3.92	1199.	381.08	3.630	60.81	4.502
	0.8250	0.5329	1.0264	0.8915	5.39	1191.	496.30	3.518	66.81	4.355

The elastic scattering of ^{6}Li on ^{12}C at 30.6 MeV was measured by Chuev *et al.* [11] and analyzed by Bassani *et al.* [12] in terms of standard optical potentials using volume Woods-Saxon form factors. The major interest in these data lie in an exotic pattern with deep Airy oscillations at intermediate angles and a substantial increase of the cross section at large angles. Similar features were observed by Vineyard *et al.* [13] in the scattering of ^{6}Li on ^{12}C at 24 and 30 MeV, ^{6}Li on ^{16}O at 25.7 MeV and ^{7}Li on ^{12}C at 34 MeV. The similarity with ALAS phenomenon is striking. Enhanced contributions to backward scattering could occur by means of exchange or heavy-particle stripping mechanisms which provides large momentum transfer in

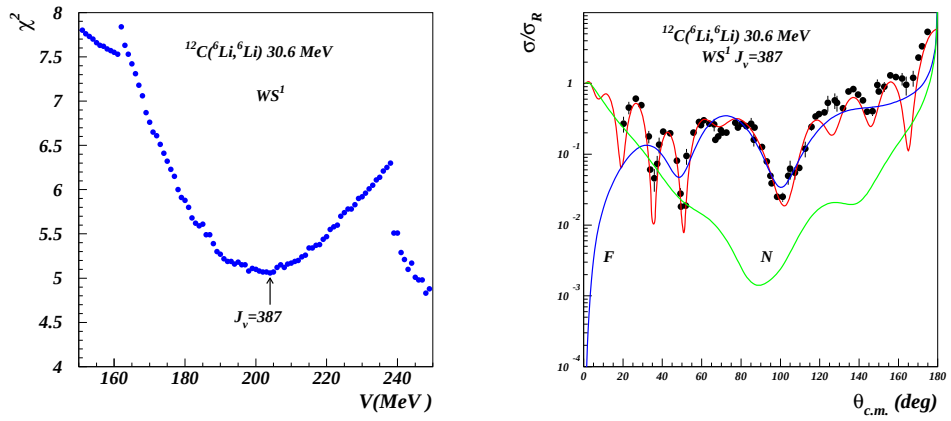

(a) (b)

Fig. 1 – (Color on-line)(a) Grid search with WS^1 form factors. At least one well defined solution. (b) F/N decomposition with WS^1 form factors. This calculation confirms the structure of the F/N components found with folding form factors.

a single scattering process. Besides the well known ^{40}Ca case, for α scattering the phenomenon was observed at the ^{16}O shell closure: ^{12,14}C, ^{14,15}N and ^{16}O all show enhanced cross section, whereas the neutron excess in ^{18}O drastically suppressed the backward scattering. According to Brink [14] the simplest explanation of ALAS could be given in terms of ordinary optical model by using strong real potentials and weak absorption. Oeschler *et al.* [15] proposed an explanation in terms of single particle resonances of potential scattering which are not damped out due to reduced absorption. Using a detailed semi-classical analysis we show that at least in this particular case the reaction mechanism is dominated by heavy ion orbiting. We start by executing a standard optical model analysis using volume Woods-Saxon form factors. The potential radii are defined in the heavy ion convention. The Coulomb component is included in the hard sphere approximation. A detailed grid search using the strength of the real potential as a control parameter revealed a single solution with real volume integral $J_v < 400$ MeV fm^3, see Table 1 and Figure 1a. There are hints for many other solutions at larger J_v values. Though the χ^2 pattern is quite large, the absolute minimum could be identified unambiguously. The corresponding real potential is very strong and absorption is weak, suggesting that the coupling with inelastic channels including breakup is quite small. The far side/near side decomposition of the scattering amplitude is shown in Figure 1b. The dominant far side component is heavy structured with a remarkable deep Airy oscillation near $\theta = 100^\circ$

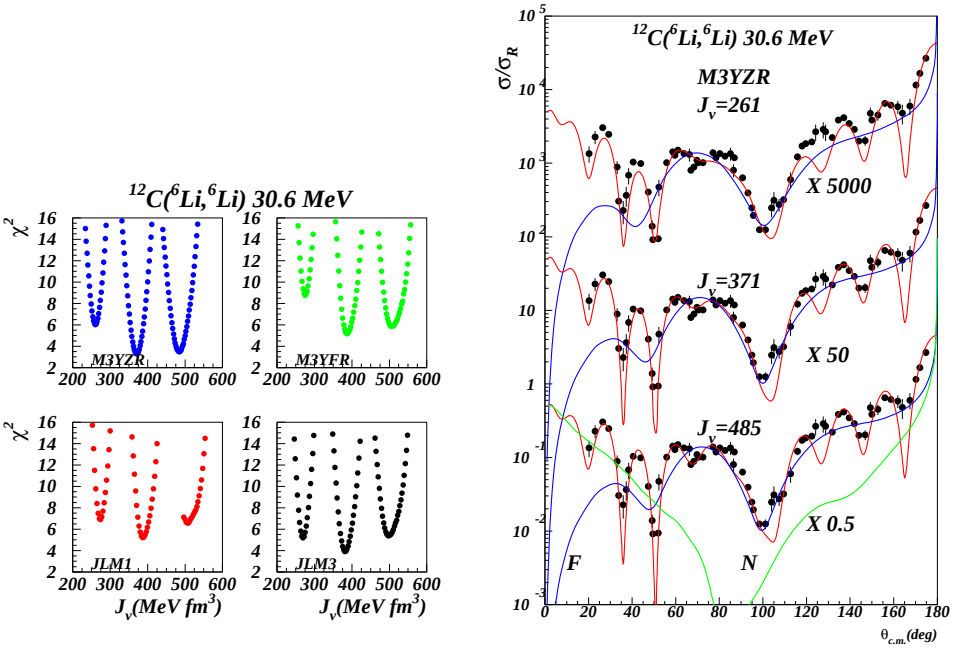

(a) (b)

Fig. 2 – (Color on-line)(a) Grid search with selected folding form factors. At least three well defined solutions for each model. (b) F/N decomposition with M3YZR. Strong refractive effects. Heavy structured far side component. Two deep Airy oscillations.

followed by oscillations of increased amplitude at larger angles.

The folding model analysis is executed using effective interactions described in our preceding paper [16] including the well known M3Y [17] in two versions (zero range and finite range knock-on exchange) as well as density dependent effective interactions GOGNY [18] and JLM [19]. The single particle densities were obtained from a standard spherical Hartree-Fock calculation using the density functional of Beiner and Lombard [20]. The obtained charge rms radii agree quite well with the systematics of Angeli [21]. Using a grid search analysis we found a number of discrete solutions see Table 2 and Figure 2a. The minima are very narrow and thus the discrete solutions are precisely defined. Examination of cross sections plotted in Figs. 2b-4b shows that these potentials are almost phase equivalent. Such equivalence was suggested to be due to the modulo π uncertainty inherent to phase determinations [9]. For deep potentials another half wavelength can accommodate in the potential well. Moreover, examination of the Table 2 shows that all folding models predict the same sequence of discrete solutions. Real volume integrals are consistent within 2%

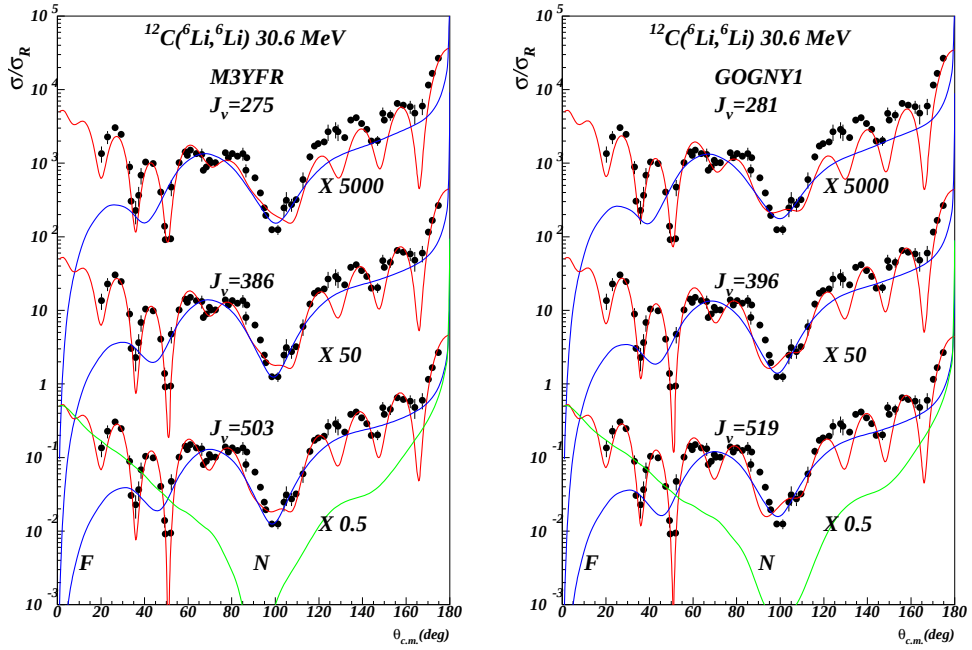

(a) (b)

Fig. 3 – (Color on-line)(a) F/N decomposition with M3YFR. (b) F/N decomposition with GOGNY1.

precision. The reaction cross section is well defined and has little variation from one calculation to another $\sigma_R = 1228 \pm 50$ mb. Although we are far from the saturation (≈ 15 MeV/A), the constant reaction cross section means simply that all important inelastic channels are already open and therefore σ_R is independent of the strength of the real potential. The major correction is needed for the imaginary range parameter t_w (of the order of 20%) in line with the Feshbach's theory of the dynamical polarization potential (DPP). At this point a remark concerning the DPP is in order. Using a CCDC calculation, Sakuragi [2] conjectured that the DPP arising from the coupling with ^{6}Li$\rightarrow \alpha + d$ breakup states is independent of target and energy and has a huge repulsive real component of the order of 40% from the bare optical potential and thus there is no need for the renormalization of the folding potential obtained from the M3Y effective interaction. However the existence of many phase equivalent discrete folding solutions with normalizations $N_v \sim 0.6 - 1$ invalidates this conjecture at least for the reaction discussed here.

The semi-classical (WKB) analysis for the decomposition of the scattering amplitude into barrier and internal barrier components starts by executing the main steps outlined in [22]. We use the WS[1] potential tabulated in Table 1 as a representative

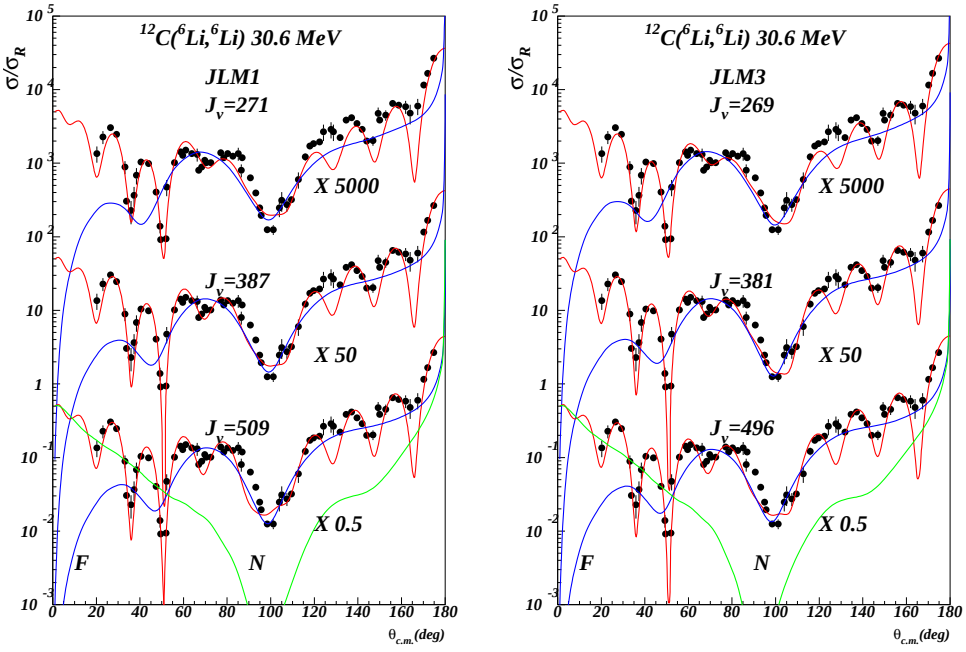

(a) (b)

Fig. 4 – (Color on-line)(a) F/N decomposition with JLM1. (b) F/N decomposition with JLM3.

potential for this reaction. The complex turning point trajectories are depicted in Fig. 5. The picture is characteristic for strong optical potentials and moderate absorption with three turning points well separated in complex plane. The inactive turning points plotted in black, are correlated with the poles of the imaginary component of the optical potential (right hand complex conjugate stars). These give negligible small contribution to the scattering amplitude. The semi-classical deflection function Fig. 6a indicates an orbiting singularity near $\ell_o = 11$ typical for strong real potentials. This is the first hint that the reaction mechanism is dominated by heavy ion orbiting. The survival elastic probability Fig. 6b shows a very large internal barrier component for all partial waves $\ell < \ell_o$ and negligible small beyond this value. Destructive interference with the barrier component produces a small Grühn-Wall spike near the orbiting momentum. The same feature is present in the exact quantum mechanical calculation (black dots in the figure). In fact we may remark that accurate calculation of the complex turning points and action integrals make the semi-classical result almost identical with the quantum mechanical result. The semi-classical scattering amplitude, decomposed into barrier and internal barrier components leads to the cross sections depicted in Fig. 7a. The barrier component which corresponds

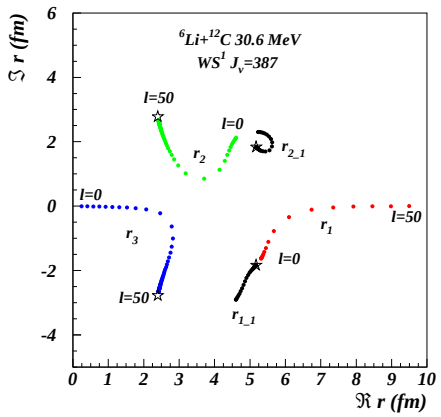

Fig. 5 – (Color on-line) Complex turning point trajectories for the WS^1 potential with the real volume integral $J_v = 387$ MeV fm^3. The inactive turning points (black) are correlated with the poles of the imaginary potential. The active turning points (blue and green) are correlated with the poles of the real potential (stars).

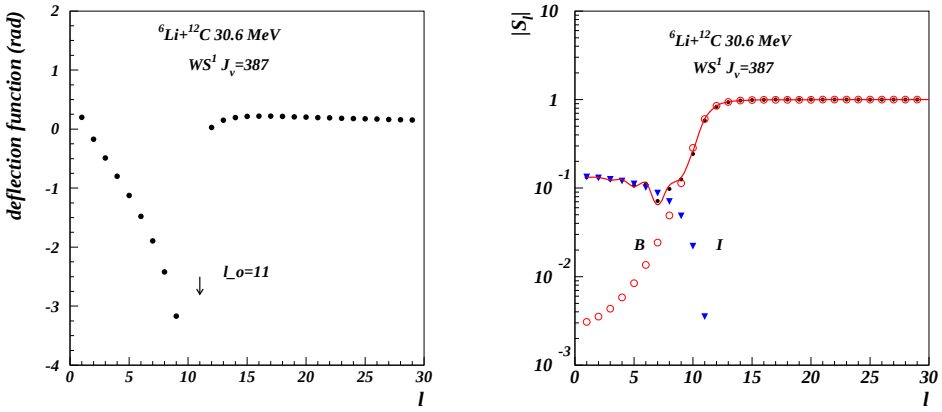

(a) (b)

Fig. 6 – (Color on-line)(a) Semiclassical deflection function. The orbiting momentum is $\ell_o = 11$. (b) The semiclassical absorption profile (red curve) is compared with the exact quantum result (black dots). The semiclassical S-matrix is decomposed into barrier (B) and internal barrier (I) components. The B/I interference produces a Grühn-Wall spike near $\ell = 8$.

to the flux reflected at the barrier has a typical diffraction pattern due to strong ab-

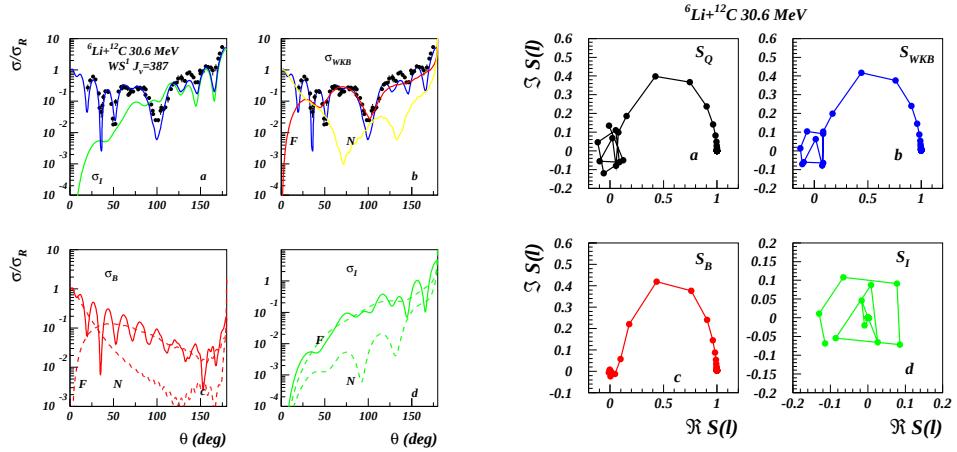

(a) (b)

Fig. 7 – (Color on-line)(a) The semiclassical (WKB) cross section is decomposed into barrier (B) and internal barrier (I) components. Each component is further decomposed into F/N subcomponents. The internal barrier component is exceptionally large and dominates the large angles. The strong B/I interference produces the deep minimum near $\theta = 100^\circ$. (b) Argand diagram for the semiclassical S-matrix. The exact quantum result (Q) is shown for comparison. The orbiting (resonant) effect is isolated into the internal barrier component (I).

sorption with large Fraunhofer oscillations at forward angles. The internal barrier component which corresponds to repeated reflections between the turning points r_3 and r_2 (Fig. 5) is responsible for the behavior of the cross section at large angles. Destructive interference of two far side components of the barrier and internal barrier amplitudes (BF and IF) leads to the deep Airy oscillation near $\theta = 100^\circ$. The Argand diagram, Fig. 7b, shows clearly the resonant effect in the low partial waves due to orbiting which is present in both total WKB and quantum S-matrix. The entire resonant effect is isolated into the internal barrier component (lower right panel). The S-matrix trajectory rotates anticlockwise around the origin several times, suggesting the presence of multiple Regge poles.

3. ^{6}LI+^{13}C AT 54 MeV

The reaction ^{6}Li+^{13}C at 54 MeV was measured [23] as a part of our long term program to find reliable ways to predict optical model potentials for reactions with radioactive beams (RNBs). In particular our interest focuses on finding reliable descriptions for transfer reactions involving relatively light, loosely bound nuclei, which are used as indirect methods in nuclear astrophysics. The stable ^{6}Li is

Table 3
Discrete solutions with WS[1] form factors for the reaction ^{6}Li+^{13}C at 54 MeV.

V	W	r_v	r_w	r_c	a_v	a_w	χ^2	σ_R	J_v	R_v	J_w	R_w
210.	15.79	0.5308	1.1474	1.0	0.8991	0.7486	3.91	1343.	325.	3.7485	115.	4.6333
306.	19.37	0.5233	1.0727	1.0	0.8268	0.8063	3.32	1365.	416.	3.5017	123.	4.5800

Table 4
Discrete solutions with folding form factors for the reaction ^{6}Li+^{13}C at 54 MeV.

pot	N_v	N_w	t_v	t_w	χ^2	σ_R	J_v	R_v	J_w	R_w
M3YZR	0.6750	0.2491	1.0796	0.7735	7.24	1503.	305.75	3.560	110.41	4.949
	0.9100	0.2591	1.1300	0.8078	4.86	1444.	413.68	3.403	115.10	4.741
	1.1450	0.2690	1.1736	0.8313	5.55	1408.	522.13	3.279	119.68	4.609
M3YFR	0.6100	0.2129	1.0751	0.7978	5.52	1454.	325.93	3.607	111.59	4.842
	0.8200	0.2228	1.1275	0.8243	5.46	1414.	439.74	3.442	116.96	4.689
	1.0450	0.2358	1.1616	0.8443	7.04	1395.	561.73	3.342	123.98	4.578
GOGNY1	0.5200	0.1773	1.0810	0.8076	5.68	1435.	333.31	3.615	111.52	4.820
	0.7000	0.1849	1.1317	0.8314	7.05	1400.	450.25	3.456	116.48	4.684
JLM1	0.5050	0.7103	1.0383	0.8094	6.04	1405.	322.18	3.575	108.71	4.810
	0.6750	0.7357	1.0867	0.8228	8.76	1389.	432.17	3.418	112.71	4.733

Table 5
Unitary solutions with Regge pole amplitudes for the reaction ^{6}Li+^{13}C at 54 MeV.

Set	L	Δ	α	β	L_1	Δ_1	D_1	Γ_1	L_2	Δ_2	D_2	Γ_2	χ^2	σ_R
R1	14.2	1.97	-2.80	-1.99	11.3	0.791	2.02	3.08	11.2	2.09	0.64	0.227	6.12	1446
R2	14.2	1.95	-2.73	-2.13	11.4	0.639	1.45	2.73	11.1	1.24	1.14	0.431	6.08	1440
R3	14.6	2.06	-2.55	-1.59	11.2	0.497	2.56	5.33	12.2	15.9	-0.78	0.0168	5.36	1427

an archetype of fragile nuclei, and produced in laboratory with sufficient intensity to allow high precision angular distributions to be measured. At energies around 10 MeV/A, the ^{6}Li interaction with light targets is moderately absorptive to allow strong refractive/resonant effects to be identified in elastic angular distribution [24]. We present here a new and dedicated analysis of these data underlying the hints for heavy ion orbiting.

A standard optical model analysis in terms of WS[1] volume potentials revealed at least two discrete solutions with real volume integrals $J_v < 450$ MeV fm^3, Table 3 and Fig. 8a. The far side/near side decomposition of the scattering amplitude is shown in Fig. 8b. The data show complex forms with characteristic rapid oscillations at forward angles (Fraunhofer) and a marked change in shape at intermediate angles: a kind of plateau followed by a very deep minimum. This feature is common for several other reactions involving ^{7}Li at similar energies [23]. Assuming pure Fraunhofer scattering at forward angles, we extract a grazing angular momentum $\ell_g = 15$ from the angular spacing $\Delta\theta = \pi(\ell_g + 1/2)$. Examination of potentials in Table 3 shows a strongly refractive core surrounded by a weakly absorptive halo. In fact the

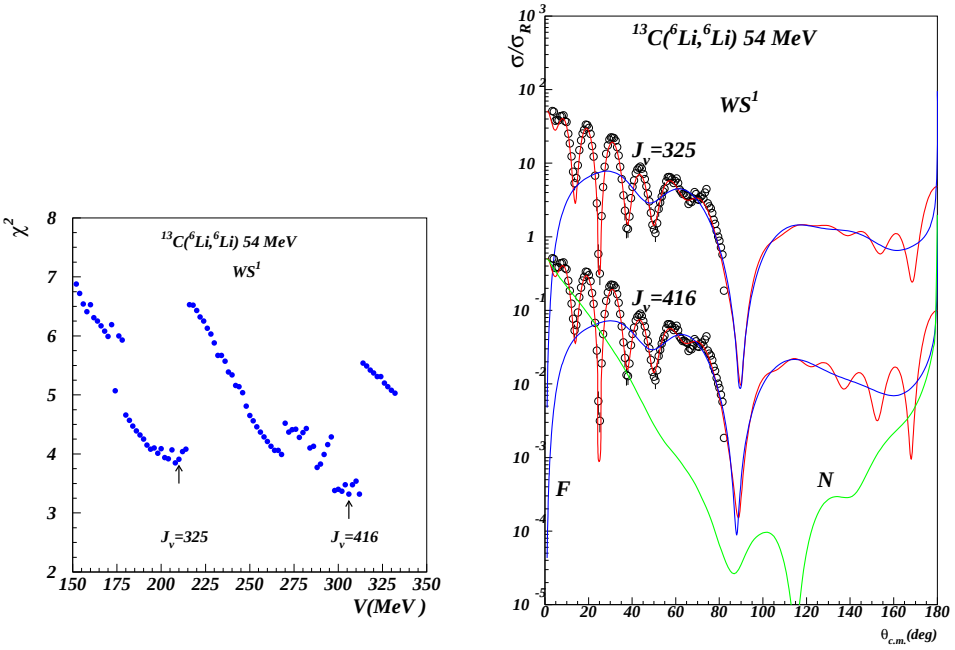

(a) (b)

Fig. 8 – (Color on-line)(a) Search for discrete solutions with WS^1 form factors. (b) F/N decomposition with WS^1 form factors. The potentials are very deep. The reaction mechanism is strongly refractive. The far side component shows a deep Airy oscillation due to a strong destructive interference barrier/internal barrier components of the scattering amplitude.

transparency parameter $w = W(r)/V(r)$ calculated at the grazing distance $\ell_g = kR_g$ is of the order of 0.1 allowing the cross section to be fully dominated by the far side component. Beyond the deep minimum near $\theta = 80^\circ$ the far side component shows a rainbow bump. Diffractive oscillations of increased amplitude due to N/F interference at very large angles are modulated by the normal increase of the far side component in this sector.

A grid search using the well known M3Y effective interaction supplemented with the one nucleon zero range knock-on exchange revealed a number of discrete solutions corresponding to normalizations $N_v = 0.7 - 1.1$ see Fig. 9. These fully equivalent solutions reflect the usual uncertainty in the phase shift determination using angular distribution taken at fixed energy. Solutions with normalizations close to unity and consistent real volume integrals are found for all effective interactions. This strengthen the conjecture that one can extract from an elastic angular distribution at best only the low rank moments of the interaction (volume integrals and rms radii).

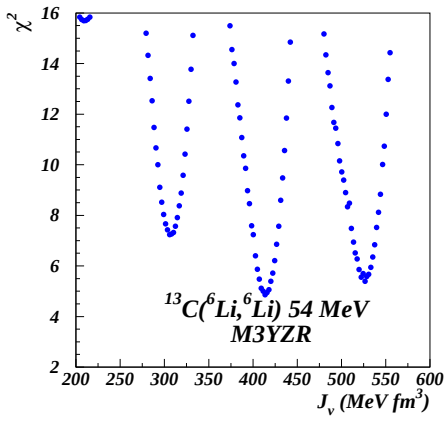

Fig. 9 – (Color on-line) Search for discrete solutions with M3YZR.

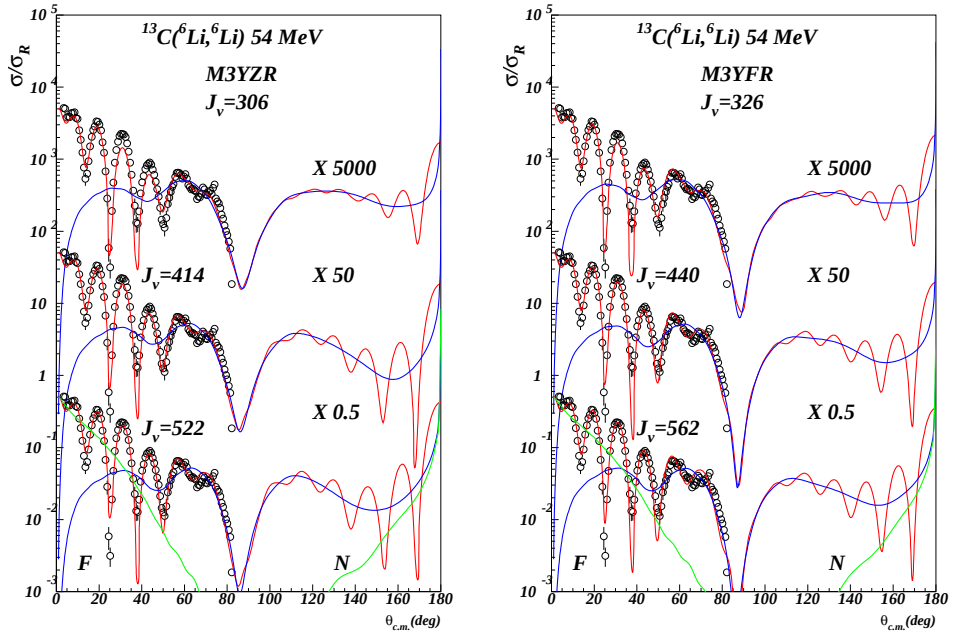

(a) (b)

Fig. 10 – (Color on-line)(a) F/N decomposition with M3YZR. The larger real volume integral, the better agreement with the data. (b) F/N decomposition with M3YFR.

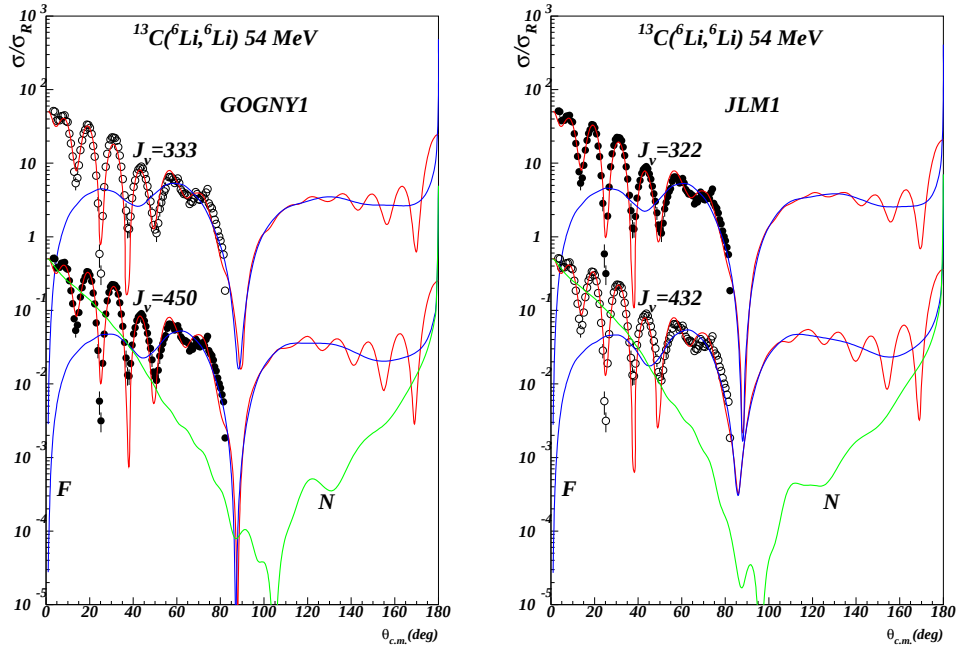

(a) (b)

Fig. 11 – (Color on-line)(a) F/N decomposition with GOGNY1. Extremely deep Airy oscillation. (b) F/N decomposition with JLM1.

This imply that one cannot determine the DPP from a coupled channel calculation by forcing a normalization $N_v = 1$. Owing to the force of circumstances (real volume integrals of the order of ~ 400 MeV fm^3 for the bare interaction) the data analysis will lead normally to $N_v = 1$ without invoking a complicated repulsive DPP if such a solution is compatible with the data. The far side/near side analysis displayed in Figs. 10a-11b shows the same heavy structure of the F/N components with deep Airy oscillations and rainbow bumps. The density dependence (pseudo zero range for GOGNY and approximately polynomial for JLM) cannot be disentangled based on the present calculation since both effective interactions GOGNY and JLM predict almost identical results, Figs. 11a and 11b. Also calculations with M3Y using a zero range knock-on exchange or exact finite range exchange give identical results. This justifies to some extent the popular use of pseudo-delta folding for exchange which avoids the tedious manipulation of nonlocal kernels.

A semi-classical (WKB) analysis based on the WS^1 potential with $J_v = 325$ MeV fm^3 is performed in order to clarify the mechanism behind the deep minimum near $\theta = 80^\circ$ and the oscillations near $\theta = 180^\circ$. The complex turning point trajec-

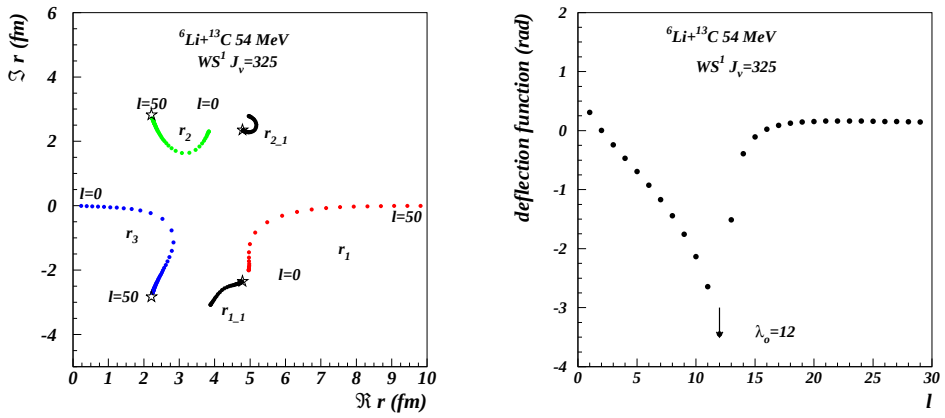

(a) (b)

Fig. 12 – (Color on-line)(a) Complex turning point trajectories for the WS^1 potential with the real volume integral $J_v = 325$ MeV fm^3. The inactive points are plotted in black. The stars are the poles of the real and imaginary components of the optical potential. (b) Semi-classical deflection function. The pattern is close to orbiting with a singularity near the orbiting momentum $\lambda_o = 12$.

tories plotted in Fig. 12a show the usual pattern with three well isolated points, an essential condition for the applicability of the Brink-Takigawa theory [25]. Since the potential is very strong, there is no surprise that the semi-classical deflection function Fig. 12b shows the usual singularity near the orbiting momentum $\lambda_o = 12$. The internal barrier component of the elastic survival probability, Fig. 13a is large for angular momenta $\lambda < \lambda_o$ and negligibly small in the rest. Practically all the essential features of the reaction are decided by the angular momentum components in this range. The strong destructive B/I interference near the λ_o produces the well known Grühn-Wall spike [26] often invoked for the increase of the cross section at backward angles. Semi-classical cross section and barrier/internal barrier decomposition are shown in Fig. 13b. The deep minimum near $\theta = 80^\circ$ appears as a destructive interference of two far side components of the barrier and internal barrier amplitudes. The forward angle sector (Fraunhofer diffraction) is entirely explained by the barrier component. This justifies the picture that the barrier component is determined by the flux reflected at the most external turning point, not penetrating the barrier. High frequency oscillations at large angles are numerical instabilities in the calculation of the corresponding action integrals. Argand diagram are presented in Fig. 14. The semi-classical (WKB) and the exact quantum result (Q) are identical. The entire orbiting/resonant effect is isolated into the internal barrier component (d) which rotates

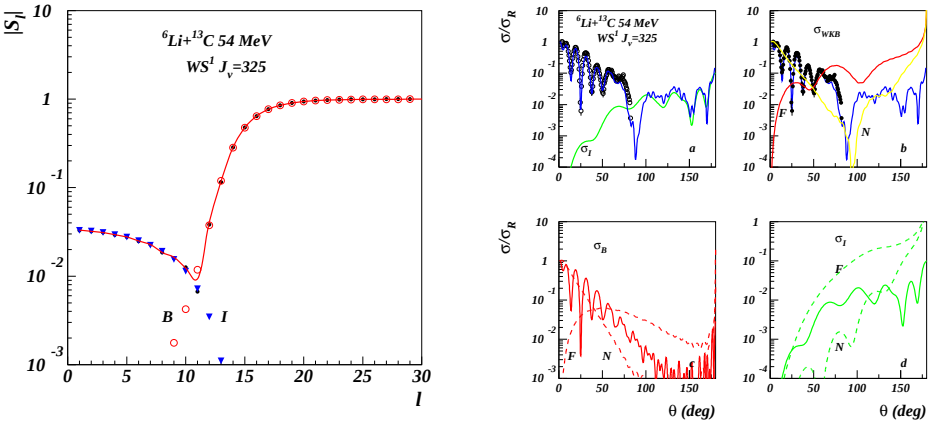

(a) (b)

Fig. 13 – (Color on-line)(a) Absorption profile. The semi-classical (WKB) profile (curve) reproduces exactly the exact quantum result (black dots). The strong B/I interference near the orbiting momentum produces a deep Grühn-Wall spike. The internal barrier component (triangles) is large as a manifestation of the refractive/resonant effects. (b) Semi-classical (WKB) cross sections F/N and B/I decomposition. The deep minimum near $\theta = 80^\circ$ appears as a strong B/I interference. As opposite to the quantum (WS) description, the rainbow bump appears here with some oscillatory structures since the internal barrier expansion of the scattering amplitude is not very reliable at large angles.

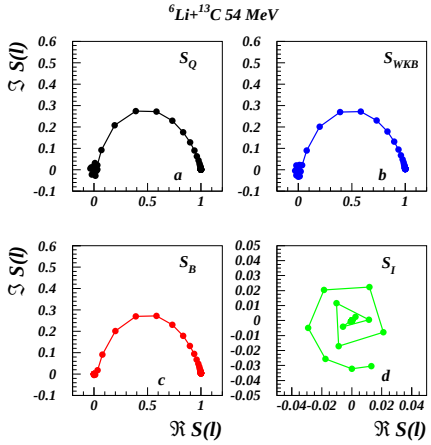

Fig. 14 – (Color on-line) Argand diagram for the semi-classical (WKB) S-matrix. The WKB pattern is identical with the exact quantum result (Q). The resonance effect is isolated into the internal barrier component (I) which rotates anti-clockwise several times around the origin.

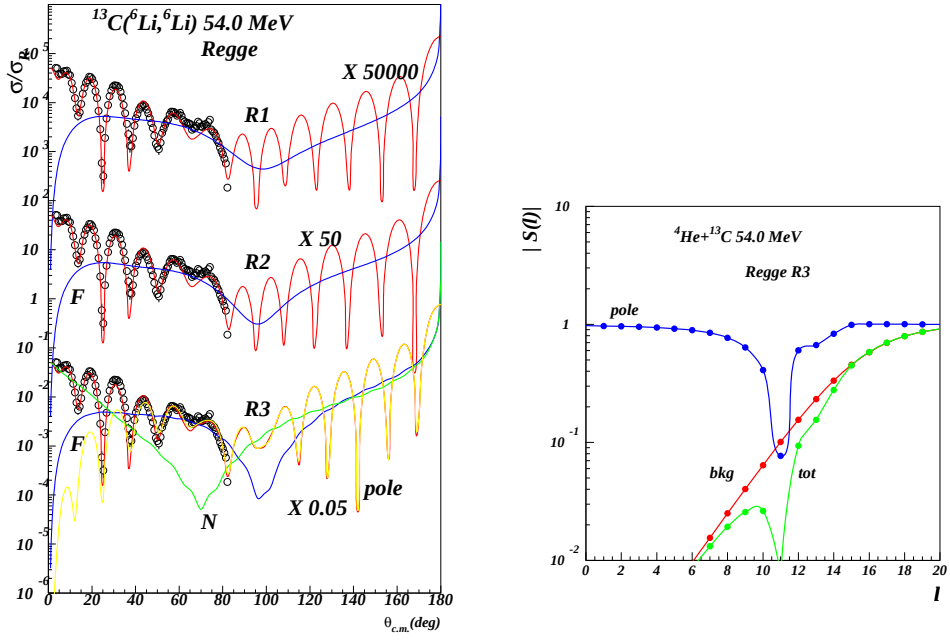

(a) (b)

Fig. 15 – (Color on-line)(a) F/N decomposition using Regge pole amplitudes. The drop in the cross section near $\theta = 80^\circ$ appears as a F/N interference. At large angles the dominant pole component shows a pattern similar to P_L^2 with angular momentum close to the orbiting momentum $\lambda_o = 12$. (b) Absorption profile using Regge pole amplitude R3. The pole component modifies dramatically the total profile. In this case the Grühn-Wall deep is carried entirely by the pole component.

anti-clockwise several times around the origin.

Three fully unitary solutions obtained with the McVoy parametrization [27] of the Regge pole scattering amplitude are tabulated in Table 5. These are obtained by constraining the background component to reproduce the reaction cross section given by the ordinary optical potential. Note that the pole component gives a small contribution to the total reaction cross section since it represents only a small (but essential) perturbation in the total scattering amplitude. In practice it is quite easy to obtain excellent non-unitary solutions, but these are rejected from obvious reasons. We also reject solutions with very large pole widths $\Gamma_{1,2}$ which exceed more than few units of angular momentum. We believe that in fact we have a unique solution in the table, the variation in the parameters reflecting merely the unavoidable parameter correlations in the highly nonlinear χ^2 minimization problem. The cross sections calculated in this approximation are depicted in Fig.15a. The pole component (yellow curve) dominates the cross section in almost all the angular range. The

background component gives an excellent description of the forward angle sector, thus confirming that the corresponding oscillations are a manifestation of diffraction due to strong absorption. At large angles the dominant pole component produces regular oscillations of the form P_{11}^2, with angular momentum close to the orbiting value $\lambda_o = 12$. The far side component of the total amplitude has the same structure as in the ordinary optical model calculation. Although the Airy oscillation is much damped, a clear signal that the mechanism is governed by diffraction due to Regge pole. The elastic survival probability is displayed in Fig. 15b for the R3 parametrization. A spectacular spike appear in the total S-matrix due to the main Regge pole localized near the real axis. Thus the legendary Grühn-Wall deep appears here as a natural effect of the Regge pole presence.

4. CONCLUSION

We have analyzed two reactions initiated by the fragile ^{6}Li on light targets in an energy window (5-9 MeV/A) in which the interaction is sufficiently strong and moderate absorptive in such a way that refractive and resonant effects are not damped by the absorption. A dedicated semi-classical and Regge pole analysis revealed typical characteristics of heavy ion orbiting. The standard optical model analysis with double folding form factors in the scaling approximation revealed a number of discrete solutions fully phase equivalent, encompassing normalization of the real form factors close to unity. This suggests that the usual calculation of the dynamic polarization potential by including coupling to the breakup channel should be revised.

Acknowledgements. This work was partly supported by CNCSIS Romania, under program PN-II-PCE-55/2011 and PN-II-ID-PCE-0299/2012, and partly by IN2P3, France.

REFERENCES

1. H. Feshbach, *Theoretical Nuclear Physics* (Wiley, New York, 1992).
2. Y. Sakuragi, Phys. Rev. **C35**, 2161 (1987).
3. P. C. Sabatier, Phys. Rev. A **8**, 589 (1973).
4. M. Cuer, Ann. Physics **120**, 1 (1979).
5. H. Leeb and E.W. Schmid, Z. Physik A**296**, 51 (1980).
6. J.J. Loeffel, Ann. Inst. Henri Poincaré **8**, 339 (1968).
7. R. Ph. Boas, *Entire Functions* (Academic Press, New York, 1954).
8. K. Chadan and P.C. Sabatier, *Inverse Problems in Quantum Scattering Theory* (2nd edn., Springer, Berlin, 1989).
9. M. Lassaut, R. J. Lombard, J. Phys. A: Math. Theor. **43**, 445210 (2010).
10. M. E. Brandan and G. R. Satchler, Phys. Rep. **285**, 143 (1997).
11. V. I. Chuev, V. V. Davidov, B. G. Novatskii, A. A. Ogloblin, S. B. Sakuta and D. N. Stepanov, Symp. on heavy-ion reactions and many-particle excitations, Saclay, 1971, contributed papers.

12. G. Bassani *et al.*, Nucl. Phys. **A189**, p.353 (1972).
13. M. F. Vineyard, J. Cook, K. W. Kemper, and M. N. Stephens, Phys. Rev. **C30**, 916 (1984).
14. D. Brink, J. Grabowski and E. Vogt, Nucl. Phys. **A309**, 359 (1978).
15. H. Oeschler, H. Fucs and H. Schröter, Nucl. Phys. **A202**, 513 (1973).
16. F. Carstoiu, M. Lassaut, L. Trache, V. Balanica, Rom. J. Phys. **61**, 400-412 (2016).
17. N. Anantaraman, H. Toki and G. F. Bertsch, Nucl. Phys. **A398**, 269 (1983).
18. D. Gogny, Proc. Int. Conf. on Nucl. Physics, Munich 1973, eds J. de Boer and H. J. Mang, Vol. 1, p. 48.
19. J. P. Jeukenne, A. Lejeune and C. Mahaux, Phys. Rev. **C16**, 80 (1977).
20. M. Beiner and R. J. Lombard, Ann. Phys. (N.Y.) **86**, 262 (1974).
21. I. Angeli, Heavy Ion Physics **8**, 23 (1998).
22. T. Al-Abdullah, F. Carstoiu, C. A. Gagliardi, G. Tabacaru, L. Trache and R. E. Tribble, Phys. Rev. C **89**, 064602 (2014).
23. Florin Carstoiu, Livius Trache, Robert E. Tribble, and Carl A. Gagliardi, Phys. Rev. **C70**, 054610 (2004).
24. Florin Carstoiu, Livius Trache, Phys. Rev. **C85**, 054606 (2012).
25. D. M. Brink and N. Takigawa, Nucl. Phys. **A279**, 159 (1977).
26. C. R. Grühn and N. S. Wall, Nucl. Phys. **81**, 161 (1966).
27. K. W. McVoy, Phys. Rev. C **3**, 1104 (1971).